A PEDOT:PSS based flexible bimodal resonant sensor with independently controllable modes

Supplementary information

Table of Contents

Experiment details

Materials

Tween 20 (>99%) and glycerophosphocholine (GPC, 98%) were bought from Macklin (China). Additionally, poly (3,4-ethylenedioxythiophene)-poly (styrenesulfonate) (PEDOT:PSS) under the trade name Clevios™ PH 1000 was procured from Heraeus Precious Metals (Germany). All these materials were utilized as received without any further purification steps.

Preparation

The preparation of modified PEDOT:PSS ink:

To prepare the PEDOT:PSS ink, 1% Tween was added to 10 mL of PEDOT:PSS solution, which was then heated and stirred on a magnetic stirring heating plate at 130 °C and 500 rpm for four hours to significantly enhance the viscosity. After cooling to room temperature, the viscosity-enhanced PEDOT:PSS ink was weighed, and 3% GPC was incorporated, followed by additional stirring at 500 rpm for 30 minutes, which further improved the ink viscosity, as shown in Figs. S1(a) and S1(b). However, during heating and stirring, some aggregation of PEDOT:PSS occurred, potentially leading to issues such as needle clogging during printing. To address this, the ink was filtered through a 0.45 μm PTFE filter and centrifuged at 3,000 rpm for 15 minutes. Post-centrifugation analysis revealed a layered ink structure, with the upper aqueous layer removed to yield a uniformly dispersed PEDOT:PSS printing ink suitable for pattern creation. Due to its hydrophilic nature, PEDOT:PSS exhibited poor adhesion to the polyethylene terephthalate (PET) substrate, necessitating pretreatment. The PET substrate was first wiped with dust-free paper moistened with deionized water, dried, and then subjected to plasma treatment, which effectively decomposed organic contaminants, cleaned, and activated the substrate surface, leading to significantly

improved adhesion, as evidenced by increased contact angles in Figs. S1(c) and S1(d).

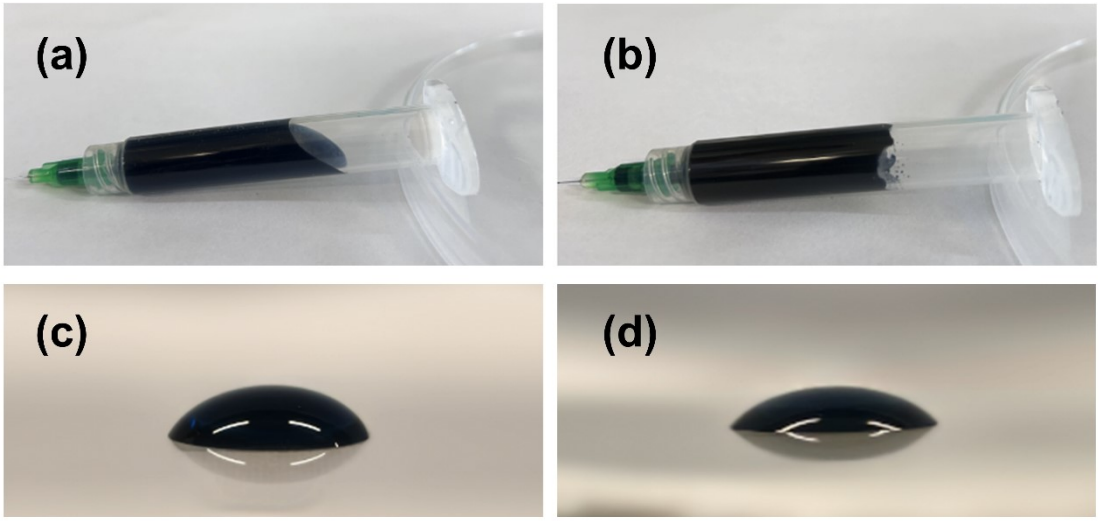

FIG s1. (a) and (b) represent comparisons conducted before and after the ink treatment. (c) and (d) illustrate the comparisons of surface contact prior to and following substrate treatment.

Due to the surface characteristics of the PET substrate, the large contact angle between the ink and the substrate resulted in poor ink adhesion and reduced pattern accuracy during inkjet printing. To address this, the substrate surface was pre-treated by cleaning with deionized water and then exposed to ozone treatment, which effectively reduced the contact angle and improved ink adhesion. The improved print quality was demonstrated by inkjet printing silver paste patterns at various resolutions (Fig. s2(a)). In addition to ink-substrate adhesion, the pressure applied at the syringe's end during printing was found to significantly affect the print outcome. Increasing the pressure from 180 kPa to 240 kPa caused the silver paste thickness to increase from 15 μm to 30 μm, with a linear correlation between thickness and the number of printed layers (Fig. s2(b)). However, a thicker silver paste layer did not necessarily improve device performance; excessive thickness resulted in material waste, higher costs, and an increased risk of cracks or fractures in the conductive layer during use. Therefore, silver paste was printed at 180 kPa, and after five layers, the thin-layer square resistance of the silver paste decreased significantly from 57 mΩ sq^{-1} to 13 mΩ sq^{-1} (Fig. s2(c)).

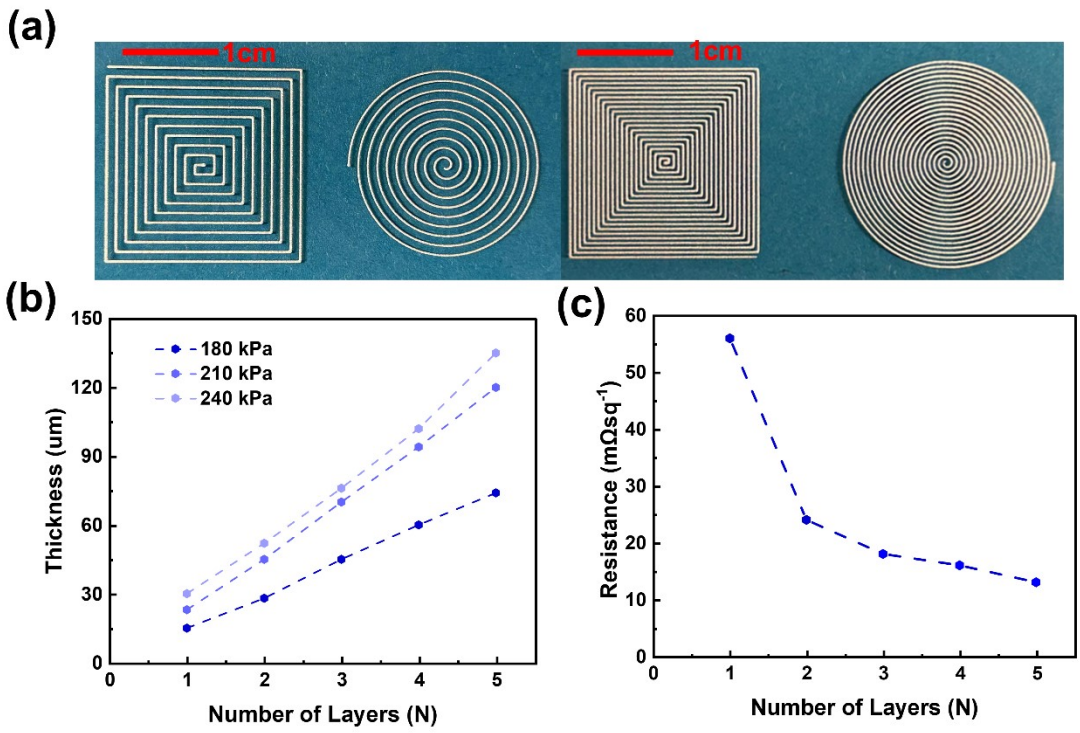

FIG s2**.** (a) Optical image of inkjet-printed stretchable silver paste, with a scale bar of 1 cm. (b) Variation in the thickness of the printed silver paste layers as a function of applied pressure during inkjet printing. (c) Relationship between the number of silver paste layers and the square resistance at an applied pressure of 180 kPa.

Rheological testing

Since silver paste is unaffected by humidity and PEDOT:PSS offers excellent electrical properties, stability, and humidity sensitivity, the latter was selected as the humidity-sensitive layer for multimodal sensing. The relatively low viscosity of commercial PEDOT:PSS solutions made it challenging to achieve strong adhesion to the silver paste layer. To address this, the PEDOT:PSS suspension was heated to increase its viscosity by evaporating some of the water content and increasing the solid content, but this process caused PEDOT:PSS to aggregate, potentially leading to nozzle clogging during inkjet printing. To improve dispersion and stability, Tween surfactant was added to the PEDOT:PSS concentrate, reducing particle interactions and ensuring more stable electrical conductivity. Additionally, the high hydrophilicity of the PSS component facilitated water absorption, and when mixed with the hygroscopic oligomer GPC, the ink's moisture absorption capacity was further

enhanced (Fig. s3). Rheological testing also confirmed that the modified PEDOT:PSS/Tween/GPC ink (PTC) was suitable for syringe printing, with a significant increase in viscosity compared to the unmodified PEDOT:PSS ink (PP) (Fig. s4(a), (b)).

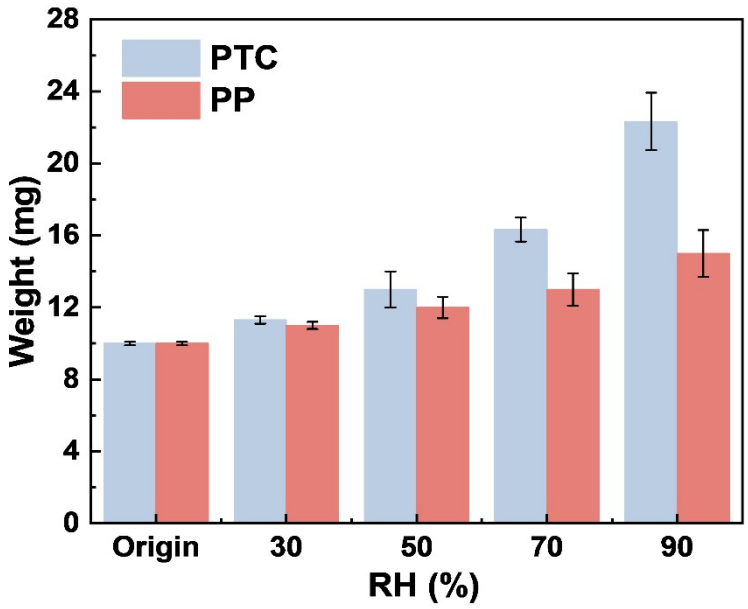

FIG s3. Comparison of moisture absorption capacity between PP and modified PTC ink.

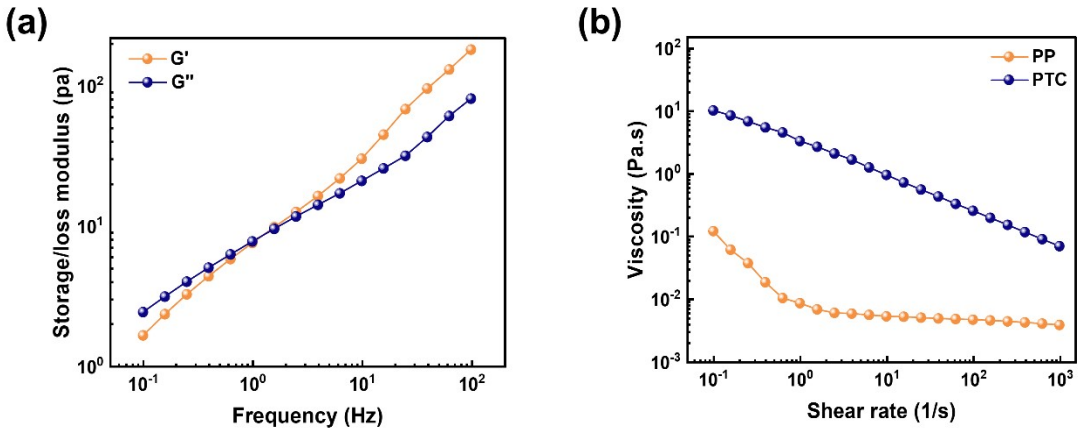

FIG s4. (a) Storage modulus and loss modulus of modified PTC ink. (b) Comparison of viscosity between PP and modified PTC ink.

Sensor fabrication and measurement:

Test environment

Following plasma treatment, the PET substrate was placed on a microelectronic printing table, where the printing process was carried out using the Musashi IMAGE MASTER 350PC Smart dispenser (MASS Co., LTD.), with the scanning speed set to 5 mm/s and a pressure of 210 kPa. The prepared ink was loaded into a syringe, which was mounted on a robotic arm, and the desired printing pattern was pre-drawn using CAD software and imported into the system. After printing, the sensor underwent curing on a heating plate at 120 °C for one hour to ensure complete ink setting. The S_{11} parameter of the antenna was evaluated using an Agilent E5071C vector network analyzer. Subsequently, the fabricated antenna sensor was soldered to a 50 Ω subminiature version A (SMA) connector and connected to the analyzer for bending and humidity testing (Fig. s5(a)). For bending tests, the sensor was affixed to cylindrical foams with varying bending radii to measure resonance frequency shifts under different bending conditions, demonstrating adaptability to bending deformations typical of wrist joints (Fig. s5(b) and s5(c)). For humidity testing, the antenna was placed inside a customized airtight box (Fig. s5(d)), with the humidity level controlled by an LY-A1 smart humidifier (from Taobao) on the right side, while a humidity sensing module within the box continuously monitored moisture levels. Resonance frequency shifts of the antenna were assessed across a relative humidity (RH) range from 30% to 90%, in 10% increments, with results showing a strong linear correlation between resonance frequency shifts and variations in both bending states and humidity levels.

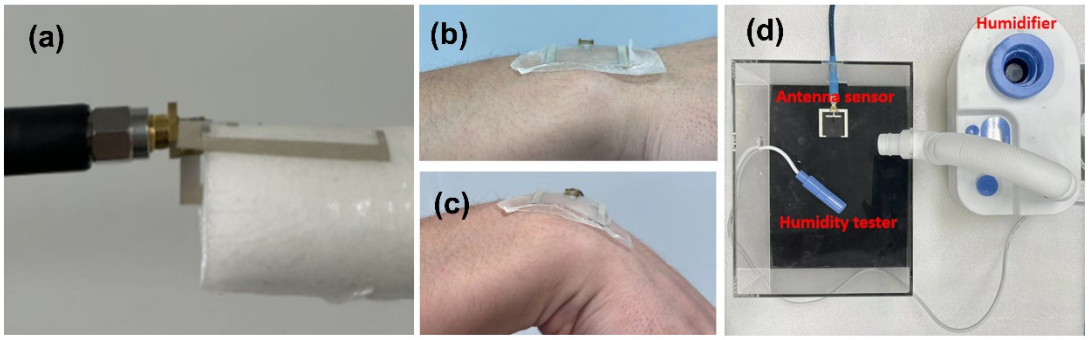

FIG s5. (a) Bending test of the antenna sensor. (b) and (c) illustrate diagrams of a bend conforming to the elbow. (d) Schematic representation of the humidity sensing test.

Mode analysis

The results of the simulation indicated that the odd-mode resonant frequency of the resonator was only controlled by L_x and Y_1, while the even-mode resonant frequency was not affected (Figs. s6(a) and s6(b)). The size of Y_1 represents the length of the lateral branches, while the change in the size of L_x represented the change in the position of the feed point, and it could be seen that with the increase in the length of Y_1, both the dual frequencies were shifted towards the lower frequencies, and the frequencies were shifted when the position of the feed point was changed.

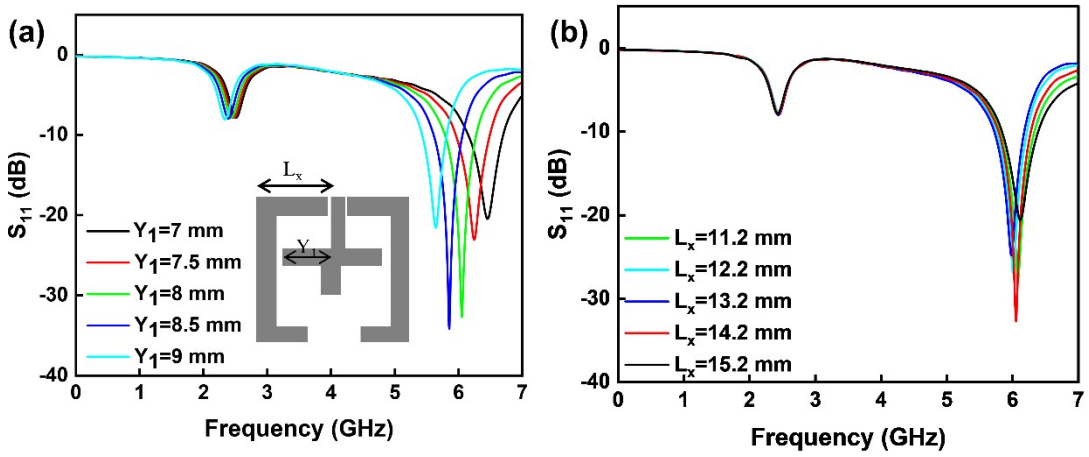

FIG s6. (a) and (b) were simulation tests conducted with varying lengths of Y_1 and L_x

Details of experiment

In order to display the test results more precisely and clearly, The resonant frequency variation curves of the sensor in the bending and humidity test environments were magnified (Figs. s7).

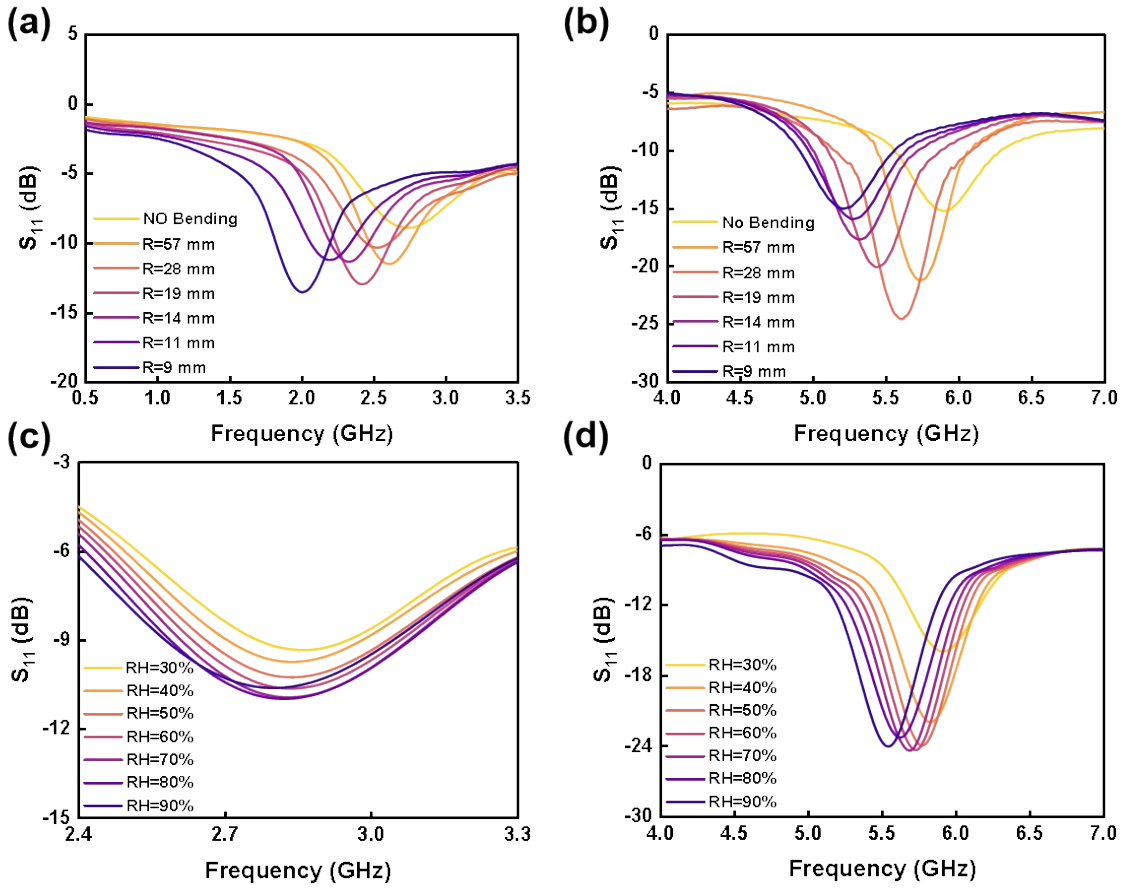

FIG s7. (a) and (b) S_{11} of the resonator as a function of bending radius. (c) and (d) S_{11} of the resonator as a function of humidity level.

Additional data and experiment

Sensor performance comparison

The comparison of the sensitivity of the resonant sensor prepared in this paper and the existing flexible antenna sensor were given in Table 1 and Table 2. It could be

seen that the sensor prepared in this paper was not only reduced size, but also had relatively high sensitivity. For the strain sensitivity, previous studies mostly used hard metals such as copper for the conductive layer, while we used stretchable silver paste. Under the same strain, the stretchable silver paste will produce a larger actual electrical length change, thereby achieving higher sensitivity. In contrast, the electrical length change of the same conductive layer under strain is relatively low. Therefore, its sensitivity is relatively low.

Table 1. The strain sensitivity of the sensor prepared in this paper was compared with that of the existing sensors

Material	Maximum sensitivity	Size (mm)	Refs.
Aluminum/paper	3.34	D=65.5 H=0.2	[1]
Copper/cellulose paper	5.39	119.4*70*0.46	[2]
Graphene/cellulose paper	9.8	119.4*70*0.46	[2]
Copper/Polyimide (PI)	24.03	62*10	[3]
Ag & PEDOT: PSS/PET	32.9	30*30*0.15	This work

Table 2. The humidity sensitivity of the sensor prepared in this paper was compared with that of the existing sensors

Material	Maximum sensitivity	Size (mm)	Refs.
Copper/Polyimide (PI)	123	370*440*400	[4]
Graphene Oxide (GO)/PI	15.2	28*84*1.4	[5]
Vertical Graphene (VG)/PDMS	2.9	30*30*2	[6]
Ag & PEDOT: PSS/PET	52.8	30*30*0.15	This work

Stability and Long-term use experiment

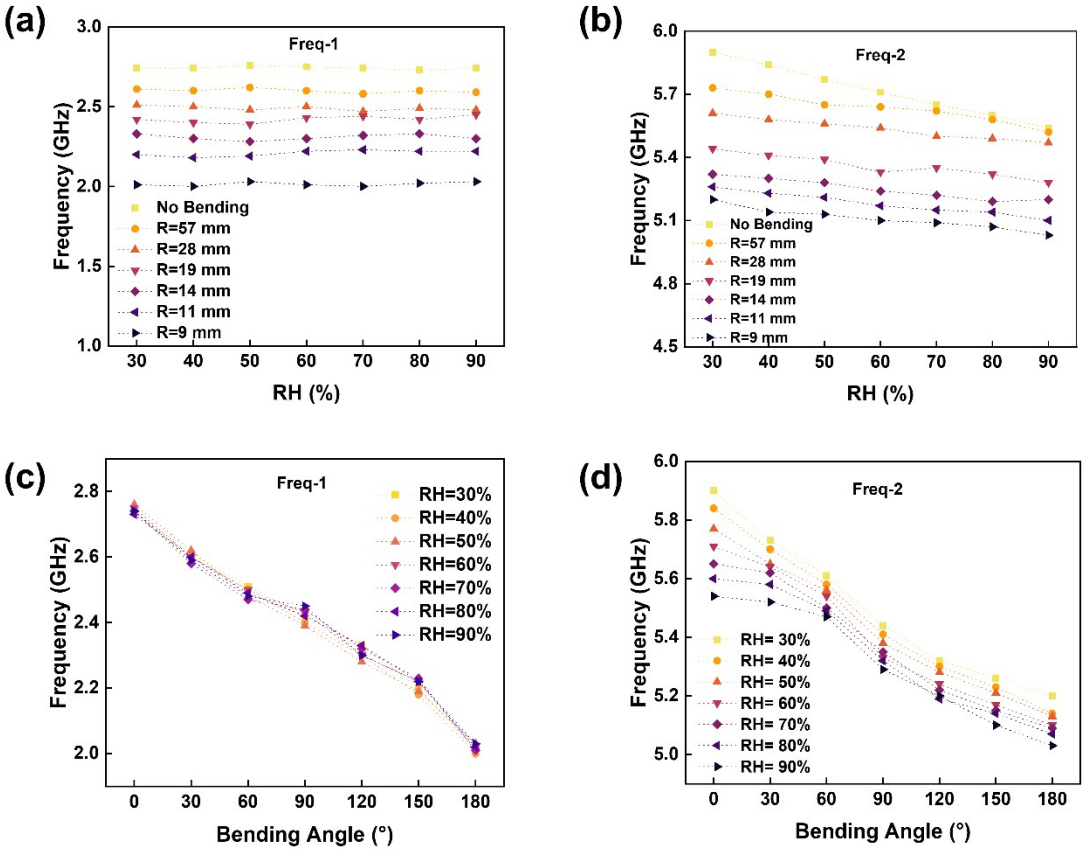

FIG s8. (a) The change of the even-mode resonant frequency with humidity under different bending radii. (b) The change of the odd-mode resonant frequency with humidity under different bending radii. (c) The change of the even-mode resonant frequency with bending angle under different humidity. (d) The change of the odd-mode resonant frequency with bending angle under different humidity.

Due to the complexity of the environment around the human body, it was often impossible to achieve a single and stable detection of strain or humidity changes. Therefore, to ensure the stable performance of the resonant sensor in a complex environment, we tested the performance of the sensor under different humidity and strain conditions (Figs. s8). These tests indicated that within the determined range, the sensing characteristics of the resonant sensor could still remain relatively stable. In addition, the long-term usage performance of the resonant sensor was also tested (Fig. s9). The data showed that the impedance matching performance (S_{11}) of the resonant sensor after long-term placement decreased. This was because the conductive layer of the sensor was exposed to the air and oxidized due to long-term placement, resulting

in poorer impedance matching. However, the resonant frequency of the sensor remained almost unchanged. Therefore, the sensing performance of the sensor was hardly affected, indicating the excellent long-term usage performance of the sensor.

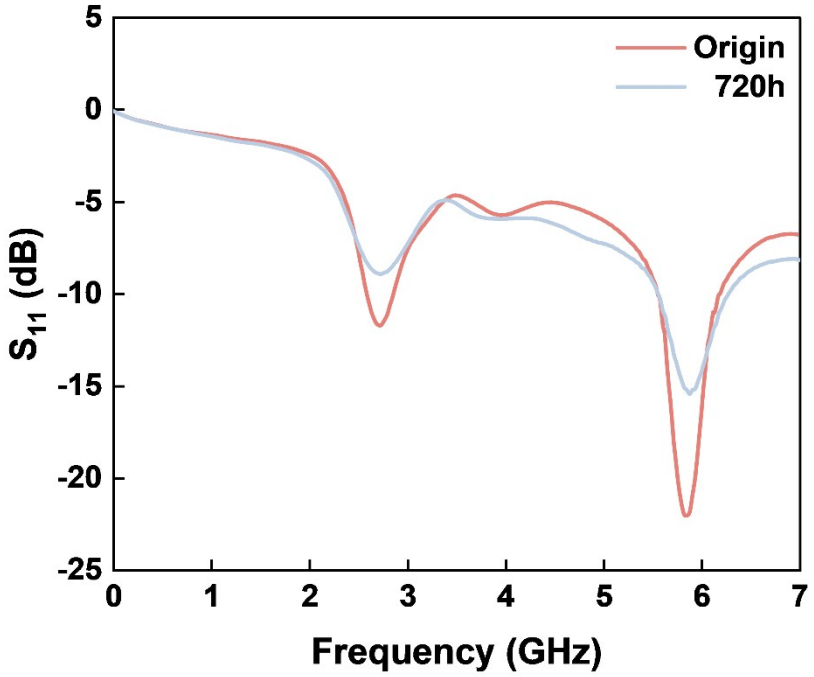

FIG s9. The comparison of the original S_{11} parameter of the resonant sensor with the S_{11} parameter after one month (720 h) of placement.

1. S. Kanaparthi, V. R. Sekhar and S. Badhulika, *Extreme Mech. Lett.*, 2016, **9**, 324-330.
2. D. Tang, Q. Wang, Z. Wang, Q. Liu, B. Zhang, D. He, Z. Wu and S. Mu, *Sci. Bull.*, 2018, **63**, 574-579.
3. J. Zhang, R. Song, X. Zhao, R. Fang, B. Zhang, W. Qian, J. Zhang, C. Liu and D. He, *ACS Omega*, 2020, **5**, 12937-12943.
4. J. Zhang, C. Li, Y. Gao, J. Tan, F. Xuan and X. Ling, *Sens. Actuators, A*, 2022, **347**, 113960.
5. H. Kou, Q. Tan, Y. Wang, G. Zhang, S. Su and J. Xiong, *Sensors and Actuators B: Chemical*, 2020, **311**, 127907.
6. X. Xuan, Z. Zhuang, Q. Shi, H. Li, C. Li and M. Li, *IEEE Internet Things J.*, 2024, **11**, 18099-18110.